PCCP

Accepted Manuscript

ROYAL SOCIETY OF CHEMISTRY

www.rsc.org/pccp

Panoscopically optimized thermoelectric performance of half-Heusler/full-Heusler based *in-situ* bulk composite $Zr_{0.7}Hf_{0.3}Ni_{1+x}Sn$: Energy and Time efficient way

A. Bhardwaj[1,2], N. S. Chauhan[1,2] Bhagyashree Sancheti[1], T. D. Senguttuvan[1,2] and D. K. Misra*[1,2],

[1]Physics of Energy Harvesting Division, National Physical Laboratory, Council of Scientific and Industrial Research, New Delhi 110012, India.

[2]Academy of Scientific & Innovative Research (AcSIR), CSIR-National Physical Laboratory (CSIR-NPL) campus, New Delhi-110012, India.

Abstract:

All scale hierarchical architecturing, matrix/inclusion band alignment and intra-matrix electronic structure engineering, so called panascopic approach in thermoelectric materials has been demonstrated to be an effective paradigm for optimizing high ZT. To achieve such hierarchically organized microstructures, composition engineering has been notified to be an efficient strategy. In this work, such panascopic concept has been extended to demonstrate for the first time in case of half-Heusler based thermoelectric materials via composition engineering route. A series of new off-stoichiometric n-type $Zr_{0.7}Hf_{0.3}Ni_{1+x}Sn$ ($0 \leq x \leq 0.10$) HH compositions have been modified to derive HH (1-x) / full-Heusler (FH) (x) composite with all scale hierarchically modified microstructure with FH inclusions within the matrix to study the temperature dependent thermoelectric properties. The structural analysis employing XRD, FE-SEM and HR-TEM of these materials reveal a composite of HH and FH, with hierarchically organized microstructures. In such submicron/nano–composite, the electronic properties is observed to be well optimized yielding a large power factor; $\alpha^2\sigma$ (~ 30.7 x 10^{-4} $Wm^{-1}K^{-2}$ for $Zr_{0.7}Hf_{0.3}Ni_{1.03}Sn$) and reduced thermal conductivity (~2.4 $Wm^{-1}K^{-1}$ for $Zr_{0.7}Hf_{0.3}Ni_{1.03}Sn$) yielding a high ZT ~ 0.96 at 773 K for composition $Zr_{0.7}Hf_{0.3}Ni_{1.03}Sn$ which is ~ 250 % larger than the normal HH $Zr_{0.7}Hf_{0.3}NiSn$ (ZT ~2.7 at 773 K) . The enhancement in ZT of

these composites has been discussed in terms of primarily electron filtering, electron injection and several phonon scattering mechanisms such as alloy scattering, point defect scattering, and grain boundary scattering. The Bergman and Fel model is used to calculate effective thermoelectric parameters of these composites for comparing the experimental results.

*Corresponding author. E-mail address: misradk@nplindia.org, dakkmisra@gmail.com (DKM)

1. Introduction:

The growing realization of economical and "clean" solid state energy conversion devices capable of competing with traditional mechanical energy conversion systems requires the ability to fabricate highly efficient thermoelectric materials with figures of merit, ZT≈3.[1] In spite of substantial increase in research output and innovative breakthroughs in this area[2-11] over the past six decades, the ability to design thermoelectric materials with ZT approaching the above targeted value has demonstrated extremely difficult mainly because of the interdependence between electronic and thermal parameters (electrical conductivity, σ; Seebeck coefficient, S; and thermal conductivity, κ) involved in dimensionless thermoelectric figure of merit, $ZT = S^2\sigma T/\kappa$. In the recent years, nanostructuring/nanocomposites,[12-17] band structure engineering,[18-21] and doping[22-25] strategies have been seen to decouple all these parameters to achieve improved figure of merit (ZT) in the state-of-the-art systems.

Among several strategies employed so far to improve ZT of conventional and emerging thermoelectric materials, nanostructuring/nanocomposite approach derived by compositional engineering approach has been demonstrated for substantial improvement in ZT due to drastic decrease in the lattice thermal conductivity (κ_l) while minimizing any adverse effect on the power factor. The mechanisms involved for phonon scattering at matrix/inclusion interfaces to reduce the

lattice thermal conductivity are now better understood.[26,27] Unfortunately, thermal conductivity reduction alone can't increase the ZT of most of thermoelectric materials to the targeted goal of ZT ≈ 3 and needs to explore the prominent strategies to combine together for decent improvement in the power factor and significant reduction in thermal conductivity simultaneously. Additionally, the power factor gain must originate from a large increase in S and descent increase in σ in order to achieve ZT ≈ 3. However such decoupling among these parameters is extremely difficult. It is therefore becoming most imperative to design some new concepts/strategies that could lead to the large enhancement in power factor through combined increase in S and σ with large reduction in κ simultaneously. More recently, a panoscopic approach which includes all-scale hierarchical architecturing mechanism for very large reduction of thermal conductivity and intra-matrix electronic structure engineering to enhance Seebeck coefficients together with optimized control of the carrier mobility with matrix/inclusion band alignment for improving the power factor has been well demonstrated in varieties of cutting-edge materials for ZT enhancement.[8,18,28-37]

Nevertheless, in spite of all these favorable features, the concept of nanocomposite stands for inherent limitation leading to deteriorating the thermoelectric properties, which have been established formerly in the light of effective medium approximation (EMA) theory by the Bergman et al.[38,39] This theory asserts that the σ and κ of a composite cannot exceed that of either best or worst thermoelectric parameters of the constituent of the composite if the contribution from the phase interface/boundary is of little worth.[38,39] The thermoelectric properties calculated by them for the binary composite indicated that the ZT of the composite could never exceed the highest ZT of each separate component phase, although enhancement in the power factor could be achieved. The proof of principle of EMA theory has been demonstrated by several researcher in various systems.[40,41] Heremans et al.[40] demonstrated this EMA theory, experimentally for a composite of Bi matrix and

inclusions of Ag. Brochin et al.[41] also demonstrated in their early experimental report that the inclusion of SiO_2 nanoparticles in polycrystalline Bi- matrix led to decreased ZT due to large reduction in σ. However, in contrary to this, several nanocomposites based on the state-of-the-art materials such as PbSe,[31,32] PbTe,[28,29,42] $CoSb_3$,[43] Bi_2Te_3,[44] Mg_2Si,[45] and HH[46] have been well demonstrated to achieve simultaneous improvement in power factor and reduction in κ yielding to an increased ZT. On the whole, it is worth mentioning that to date high ZT in these nanocomposites was observed due to primarily drastic reduction of the lattice thermal conductivity (κ_l).

Most of the emerging state-of-the-art thermoelectric materials explored so far are toxic and expensive. The half-Heusler compounds (with general compositions MNiSn (n-type) and MCoSb (p-type); where M= Zr, Hf, Ti) are more environmentally benign, and hence continuously attracting tremendous amount of interest in thermoelectric research. However, limited progress has been made due to a large variation in reported properties. For instant a report of ZT~1.5 at 700 K for $Ti_{0.5}Zr_{0.25}Hf_{0.25}NiSn_{0.998}Sb_{0.002}$ [47] obtained with S = -350 μVK^{-1}, ρ = 2mΩ cm and κ = 3Wm^{-1} K^{-1}. It is worth noting that only one or two of these favorable properties have been reproduced by other groups[48] but never all three in this composition. This irreproducibility was attributed to the lack of complete structural determination.[46(h)] Though, HH compounds are narrow gap semiconducting thermoelectric and have non-parabolic band features near the Fermi level which facilitate to exhibit high thermoelectric power-factor PF (=$S^2\sigma$). However, the ability to synthesize half-Heusler based materials with appreciable thermoelectric figures of merit, ZT (= (PF/ κ)*T) has been jeopardized by their very large thermal conductivities (κ; typically between 5 W/mK to 10 W/mK) in comparison to that of the state-of-the-art TE materials.[49]

In past decades, solid-solution alloying, controlled doping, and nanostructuring/nanocomposite approaches have also been adopted in half-Heusler compounds to reduce their thermal conductivities

by disrupting the heat carrying phonons.[46] Further, FH inclusions embedded in the HH matrix resulting via phase segregation in off-stoichiometric (Ti,Zr,Hf)Ni_{1+x}(Sn,Sb) composition[46a-46h] has been demonstrated exhibiting significantly low thermal conductivity without influencing the electronic transport. This reduction in thermal conductivity was ascribed to various scattering mechanisms such as alloy scattering due to large difference in atomic mass of the present elements,[50] point defect scattering due to embedded nanoparticles,[51] and promoted grain boundary scattering due to nano- and micro-structuring.[52]

It is worth mentioning that very large reduction in thermal conductivity can be realized in a very recent approach so called "a panoscopic approach" which includes all-scale hierarchical architecturing mechanism, originating various interesting phenomena such as very large reduction of thermal conductivity, enhanced Seebeck coefficients due to intra-matrix electronic structure engineering, and optimized control of the carrier mobility via matrix/inclusion band alignment.[28-37] The relevance of all these important mechanisms have been further demonstrated by Biswas et al.[53] in a combined approach so called ''panoscopic'' strategy to disrupt heat-carrying phonons across integrated length scales to produce a ZT = 2.2 at 915 K in PbTe–SrTe compound.[53] Intra-matrix electronic structure engineering and matrix/inclusion band alignment are together known as band-structure engineering approach that exploits the structural similarities between the matrix phase and inclusion phase to create matrix/inclusion interface with an alignment or offset of their valence band (VB) and/or conduction band (CB) favorable for optimization of the carrier mobility. Band structure engineering has been successful demonstrated to optimize high ZT of many state-of-the-art thermoelectric materials.[50,52,53]

In the present work, taking the advantage of HH and FH crystal structures, their atomic arrangement and their structural similarity, a particular new undoped off-stoichiometric half-Heusler

$Zr_{0.7}Hf_{0.3}Ni_{1+x}Sn$ compositions have been derived by the tunable compositional engineering approach in order synthesize a composite of HH phase containing FH inclusions with various length scales. The compositions synthesized are free of doped Sb & Bi. Many exciting mechanisms originated due to various length scale of FH inclusions in these composite to modify the electronic and thermal transport based on the panoscopic approach were seen to have been observed. A decent value of ZT= 0.96 at 773 K was optimized due to simultaneous improvement of power factor and reduction in thermal conductivity for a particular composition $Zr_{0.7}Hf_{0.3}Ni_{1.03}Sn$.

2.0 Experimental Details:

2.1 Materials Processing

The compositions $Zr_{0.7}Hf_{0.3}Ni_{1+x}Sn$ (with x= 0, 0.03, 0.05 and 0.1) were synthesized by direct arc-melting of zirconium, (Zr; 99.99%, Alfa Aesar, powder), hafnium (Hf; 99.99%, Alfa Aesar, powder) nickel (Ni; 99.99%, Alfa Aesar, powder), and tin (Sn; 99.99%, Alfa Aesar powder) in their exact stoichiometric compositions. The entire melted ingot was then annealed at 1073 K for one week under vacuum in a quartz tube for stabilization of phases to get a homogeneous phase. The ingots were then subsequently broken into small pieces and grounded to a fine powder by using mortal and pastle. These powders were further blended employing planetary high energy ball milling to obtain very fine powders prior to spark plasma sintering (SPS). The resulting fine powders were then consolidated employing SPS at temperatures of 1073 K and pressure of 50 MPa for holding time of 10 minutes using graphite die of 12.7 mm diameter to get 12.7 mm diameter bulk dense pellets. Under these synthetic conditions, bulk submicron/nano-composite samples containing the various fractions of FH submicron/nano-inclusions embedded within the bulk HH matrix were obtained accordingly with the chemical Eq. 1:

$0.7Zr + 0.3Hf + (1+x)Ni + Sn \longrightarrow (1-x)\ Zr_{0.7}Hf_{0.3}NiSn(HH) + x\ Zr_{0.7}Hf_{0.3}Ni_2Sn(FH)$.....(1)

The obtained bulk dense pellet samples were cut into two pieces, one is in the form of bar about 2x3x10 mm^3 and another one is 12.7 mm diameter discs which were used for measuring the electronic and thermal transport respectively.

2.2 Phase and Microstructural Characterization:

The phase identification of $Zr_{0.7}Hf_{0.3}Ni_{1+x}Sn$ (with x= 0, 0.03, 0.05 and 0.1) samples were carried out by powder X-ray diffractometer (XRD; Rigaku Mini Flex II) in reflection θ- 2θ geometry, with position sensitive detector (Ultafast D Tex), operating at 30 kV and 20 mA, using a graphite monochromator and CuK_α radiation with wavelength $\lambda \approx 1.5406$ Å along with $CuK_{\alpha 2}$ filter and rotating anode equipped with powder 2θ diffractometer ranging from 20 to 80 degrees. In order to avoid errors in experiments, all the samples were subjected to same experimental conditions and parameters such as sample size, power ratings of X-ray tube (30 kV, 20 mA) and other diffractometer parameters such as scan speed, counting steps etc. for all diffraction experiments. The microstructure investigation of all the samples was carried out by field emission scanning electron microscopy (FE-SEM; Model: SUPRA40 VP) operating at 30 KV and transmission electron microscopy (TEM, Technai G^2T^{30}; W-Twin) operating at 300 KV. The TEM specimens were prepared in three steps and described elsewhere.[14,15,17] The composition and elemental analysis of the samples were performed using energy dispersive spectroscopy (EDS) attached to the FE-SEM.

2.3 Thermoelectric Properties

Thermal diffusivities of $Zr_{0.7}Hf_{0.3}Ni_{1+x}Sn$ (with x= 0, 0.03, 0.05 and 0.1) composite samples were measured by using a laser flash system (Lineseis, LFA 1000) on disk-shaped specimens with approximate thickness of 2.0 mm and diameter of 12.7 mm. The disc specimens used for thermal

diffusivity were sprayed with a layer of graphite in order to minimize errors due to emissivity. Specific heat was determined by a differential scanning calorimetry (DSC) instrument (822^e Mettler Toledo). The thermal conductivity of composites was calculated using the relation, $\kappa = d \times Cp \times \rho$ where d is the thermal diffusivity, ρ the geometrical pellet density and Cp the heat capacity. The Seebeck coefficient and resistivity were measured simultaneously employing commercial equipment (ULVAC, ZEM3) over the temperature range of 300 K to 773 K on samples of polished bars of about $3 \times 2 \times 10$ mm^3.

3.0 Results and Discussions:

3.1 X- ray Diffraction Analysis:

The power XRD patterns of the submicron/nano-composites of HH(1-x)/FH(x) derived from compositions $Zr_{0.7}Hf_{0.3}Ni_{1+x}Sn$ (with x= 0, 0.03, 0.05 & 0.1) are shown in fig. 1. The X-ray diffraction analysis of $Zr_{0.7}Hf_{0.3}Ni_{1+x}Sn$ composition with x=0 clearly reveals the presence of peaks of HH (Fig. 1a) (space group $F\bar{4}3m$; no. 216) ; JCPDS card No # 00-023-1281) without any trace of secondary phase. However, the XRD patterns of $Zr_{0.7}Hf_{0.3}Ni_{1+x}Sn$ with increasing x exhibit prominently half-Heusler phase together with additional peaks corresponding to FH phase (*Fm3m*; no. 225; JCPDS card no. 00-023-1282). The excess Ni taken in all the composites in the present investigation were below the solubility limit of Ni in HH phase as reported by Chai et al.[54] The unit cell constants were refined by the POLSQ FORTRAN program.[55] The lattice parameter of HH was computed to be $0.594 \pm 0.513 \times 10^{-4}$ nm in composition $Zr_{0.7}Hf_{0.3}Ni_{1+x}Sn$ with x=0 using POLSQ FORTRAN program.[55] On the other hand the lattice parameter of the HH phase in HH(1-x)/FH(x) composite samples is slightly larger than those reported in the literature[56] and increases with increasing x i.e. increases with increasing FH fraction in $Zr_{0.7}Hf_{0.3}Ni_{1+x}Sn$ following the Vegard's

law as shown in fig 1(b) which is consistent with earlier reports.[46(a)-46(g)] However, the computed unit cell parameter of the full-Heusler phase in these composites is noticed to be slightly smaller than the reported value.[57] We do not find obvious increasing trend of lattice parameter of FH with increasing FH fraction (fig 1(c)) similar to other reports.[46(a)-46(g)]

It is well known that the compositional variation in most of the half-Heusler based materials HH usually results in a miscibility gap in liquid, which allows a phase separation[58] At high temperature in arc melting itself, the liquid melt of $Zr_{0.7}Hf_{0.3}Ni_{1+x}Sn$ undergoes solidification at low temperatures and crystallizes to form a single solid solution of HH and FH. During cooling at low temperature, this solid solution further decomposes into stable mixture consisting of HH and FH via phase separation similar to the observation of Chai et al.[58c] It may be noted that the decomposition of the phases occurred via phase separation might have originated due to random mixture of Ni atoms and the presence of the fourth fcc sub-lattices in HH and FH. In this process of phase separation, HH phases were formed through decomposition of fourth fcc sub-lattice into vacant site while, occupying the fourth fcc lattices with Ni gives rise to the formation of FH as presented in schematic of unit cell in figure 2. For more clearly visualized understanding, the unit cell structures of HH and FH are also presented. The unit cell of HH (Zr, Hf)NiSn as shown in fig. 2(a) contains four (Zr, Hf) atoms in the 4b positions (1/2, 1/2, 1/2), four Sn atoms in the 4a position (0, 0, 0), and four Ni atoms in the 4c position (1/4, 1/4,1/4). The structure, therefore, consists of four interpenetrating fcc-lattices: a lattice of Ti atoms and a lattice of Sn atoms forming a rock salt structure, a lattice of Ni atoms occupying the centers of every other cube, and an ordered lattice of vacancies. This ordered vacancies are filled by Ni atoms in 4c position (1/4, 1/4, 1/4) to form a full-Heusler structure as shown in fig 2(b). A combined HH and FH phase structure resulting via phase separation is also shown in fig 2(c).

3.2 Microstructural Characterization:

In order to identify the composition of phases and morphological details, scanning electron microscopy (SEM) and transmission electron microscopy (TEM) investigation of HH (1-x)/FH(x) composites in compositions $Zr_{0.7}Hf_{0.3}Ni_{1+x}Sn$ ($0.0 \leq x \leq 0.10$) have been performed. The SEM morphologies of all the HH(1-x)/FH(x) composites in compositions $Zr_{0.7}Hf_{0.3}Ni_{1+x}Sn$ ($0.0 \leq x \leq 0.10$) are shown in the supplementary material (fig. S1).

Transmission electron microscopy (TEM) of $Zr_{0.7}Hf_{0.3}Ni_{1.03}Sn$ submicron/nano-composite has been carried out to see the microstructure and internal structure. The bright field electron micrographs obtained from the specimens of $Zr_{0.7}Hf_{0.3}Ni_{1.03}Sn$ submicron/nano-composites is displayed in fig. 3(a). A clear two phase contrast with black and dark grey appearance can be discerned. The EDAX-SEM analysis which is shown in the supplementary information clearly confirms the black contrast to be FH and dark grey as HH phase. One can also clearly see the uniform distribution of various length scale FH inclusions into the HH matrix. Interestingly, one of area marked by rectangle box in fig 3(a) shows FH inclusions grown endotaxially into the HH matrix through nanoscale precipitation process similar to the other reports[27-30,46(a)-46(f)] which is displayed in the inset of fig 1(a). In order to see the finer microstructure details of the best performing composite $Zr_{0.7}Hf_{0.3}Ni_{1.03}Sn$, a high magnification TEM image is shown in fig 3(b). Interestingly, a lattice resolution features and an evidence of coherent interfaces between HH and FH (marked by rectangle area) can be seen in fig 3(b) showing excellent crystalline. The HRTEM obtained from a region marked by dotted rectangle (fig. 3(b)), reveals a clear evidence of coherent interface between the FH and HH i.e. inclusions/matrix interface. The spacing between the lattice planes of HH and FH are found to be ~ 0.35 nm and ~ 0.365 nm, which corresponds to lattice plane of (111) for HH and FH phases respectively. Also, through the use of chemical equation 1, we claim that these inclusions are FH phase. In the view of structure-physical property correlation, these multiple length scale FH inclusions distributed in the HH matrix are

expected to influence the electron and phonon transport properties. The coherent interfaces between the HH matrix and the FH inclusion phases (fig. 3(b)) are expected to promote charge carrier transfer across the matrix/inclusion interfaces which will be discussed in the forth coming part of the manuscript.

3.3 Electronic Transport Properties

Temperature dependent electronic transport behavior of HH(1-x)/FH(x) composites in compositions $Zr_{0.7}Hf_{0.3}Ni_{1+x}Sn$ ($0.0 \leq x \leq 0.10$) is displayed in figure 4. All the samples exhibit negative values of the Seebeck coefficient indicating n-type semiconducting behavior (fig. 4a). At 323 K, the Seebeck coefficient of HH(97%)/FH(3%) composite in composition $Zr_{0.7}Hf_{0.3}Ni_{1.03}Sn$ is -123 μV/K (figure 4a) which is ~73 % increase as compared to the value of ~ -71 μV/K obtained for the bulk $Zr_{0.7}Hf_{0.3}NiSn$ (HH) matrix. The Seebeck coefficient of HH(97%)/FH(3%) composite increases with temperature reaching a maximum value of -157 μV/K at 773 K which is ~50 % higher than the Seebeck coefficient of the bulk HH matrix (α ~ -104 μV/K at 773 K). However, the Seebeck coefficient of HH (95%)/FH(5%) composite was observed to be -80 μV/K at 323 K which is ~12 % higher than the value of Seebeck coefficient measured for bulk HH matrix (α ~ -71 μV/K at 773 K).. On the other hand, for HH (90%)/FH (10%) composite, the Seebeck coefficient was noted to be significantly low (i.e. -13 μV/K at 323 K) indicating the composite to be more likely a metallic or semi-metallic in nature.

The observed large increase in the Seebeck coefficient of HH(1-x)/FH(x) composites in $Zr_{0.7}Hf_{0.3}Ni_{1+x}Sn$ with x=0.03 and 0.05 compared to the bulk HH matrix are consistent with their respective decrease in the carrier densities (n) (table 1). For instance, a nearly 3-fold reduction (from $4.9x10^{19}$ cm^{-3} for the bulk HH matrix to 1.7 x 10^{19} cm^{-3} for HH(97%)/FH(3%) composite with composition $Zr_{0.7}Hf_{0.3}Ni_{1.03}Sn$) in the carrier density was observed at room temperature for the

$Zr_{0.7}Hf_{0.3}Ni_{1.03}Sn$ composite (table 1). This is a quite surprising result. Normally, upon introducing metallic FH inclusions within a semiconducting HH matrix, one should expect an increase in the carrier density of the resulting composite if the matrix is electronically doped by the inclusion phase.[46(c)] We therefore attribute the observed large reduction in the carrier density of the HH(1-x)/FH(x) composites in $Zr_{0.7}Hf_{0.3}Ni_{1+x}Sn$ with x=0.03 and 0.05 around 323 K is due to the filtering (trapping) of low energy carriers by energy barriers (ΔE) generated at multiple length scale phase boundaries between the HH matrix and the FH inclusions (figure 5) similar to the model proposed by Faleev et al.[59] and experimentally observed reports.[46(a)-46(f)] In this model, band bending at the metallic inclusion/matrix interfaces induces a potential barrier that acts as an energy filter for low energy electrons, while high energy electrons remain almost unaffected. This large reduction in the carrier concentration leads to significant increase in the Seebeck coefficient similar to the earlier reports of various HH/FH composites.[46(a)-46(i)]

A plausible explanation of the increasing α in $Zr_{0.7}Hf_{0.3}Ni_{1+x}Sn$ with x=0.03 and 0.05 as compared to bulk HH sample may also be discussed in terms of a model involving the scattering factor and reduced Fermi energy proposed by Nolas et.al.[60] where α is expressed as:

$$\alpha = \frac{\pi^2}{3}\frac{k_B}{e}\left(r + \frac{2}{3}\right)\left(\frac{1}{\xi}\right) \quad \text{.....(2)}$$

Where k_B is the Boltzmann constant, r is the scattering factor and ξ is the reduced Fermi energy. The decrease in the carrier concentration of HH(1-x)/FH(x) composite in $Zr_{0.7}Hf_{0.3}Ni_{1+x}Sn$ with x=0.03 and 0.05, may reduce the Fermi energy and consequently result in an increased α as compared to normal HH $Zr_{0.7}Hf_{0.3}NiSn$ sample. Additionally, the increase in α of $Zr_{0.7}Hf_{0.3}Ni_{1.03}Sn$ sample may also be attributed to an increased scattering factor r, apparently from the potential barrier scattering effect.[61] Nevertheless, further studies may be required to understand the mechanism leading

to increase in the scattering factor and the electron filtering effects. Thus, it appears that the overall effect of metallic multiple length scale FH inclusions on the electronic transport of HH(1-x)/FH(x) composites might be related to several factors, such as optimum size, the carrier concentration, potential profile in the bulk matrix and the position of the Fermi level compared to bulk HH. Usually in semiconductor, the simultaneous increase in σ and α is not expected and would require a high temperature Hall measurement to have better understanding.

Consistent with increase in Seebeck coefficient of the composites namely, HH (97%)/FH (3%) and HH (95%)/FH (5%) at room temperature, the decrease in the electrical conductivity of these composites was also noticed. However, surprisingly the electrical conductivity of the $Zr_{0.7}Hf_{0.3}Ni_{1.03}Sn$ composite (3% FH) at 323 K is only ~8% lower than that of the bulk HH-matrix (Figure 4b) despite the measured large decrease in the carrier densities. This marginal decrease in the σ despite of large decrease in the carrier concentration is compensated by a large increase in the mobility. This surprising increase in mobility presumably results from the reduction in the frequency of electron-electron collision arising from the large decrease in the "effective" carrier density around 300 K. Interestingly, the electrical conductivity rapidly increases with temperature outperforming the bulk HH matrix around 473 K. At 773 K, the electrical conductivity of the HH (97%)/FH(3%) composite is ~12.3 x 10^2 S m^{-1} which is ~20% higher than that of the bulk HH matrix value of ~ 10.3 x 10^2 S m^{-1} (figure 4b). The decrease in the electrical conductivity of HH (1-x)/FH(x) composite containing 5 % FH inclusion was also observed at room temperature which is about ~5% in comparison to that of bulk HH. Thus, we attribute that the reduction of electrical conductivity at room temperature for HH (1-x)/FH(x) composite containing FH inclusions of 3 % and 5 % is due to filtering of low energy electrons at the HH/FH interfaces. The temperature dependent variation of electrical conductivity for HH(1-x)/FH(x) composites indicate that electrical conductivity increases

with rising temperature for samples upto x=0.05 revealing the semiconducting behavior of the samples. However, the electrical conductivity of (HH (90%)/FH (10%) composite with composition $Zr_{0.7}Hf_{0.3}Ni_{1.10}Sn$ decreases with increasing temperature exhibiting metallic behavior. The room temperature measurements of the Hall coefficient (R_H) were used to determine a Hall carrier concentration ($n=1/R_H\ e$) for all the HH (1-x)/FH(x) composites. Further, the room temperature electrical conductivity, and carrier concentration n are used to calculate the room temperature mobility (μ) by a relation $\sigma = ne\mu$ (where n is the carrier concentration, e is the charge of an electron and μ is the carrier mobility) and results are shown in table 1.

For better visual understanding of transport properties related to band bending effect, the alignment of the HH and FH at the HH/FH interfaces is illustrated in figure 5. It is worth noting that band structure of FH phase is related to that of the HH phase because of similar composition and differs only because of presence of a partially filled band with Ni; being on the top of FH valence band. This additional Ni on the top of the FH valence band induces the top of the valence band maxima (VBM) and conduction band minima (CBM) of FH phase to be pushed up to higher energy as compared to that of the corresponding HH phase. The same has been presented in molecular orbital theory (MOT) diagram (fig 5a). Through this MOT, one can anticipate the formation of a hetrojunctions (staggered gap) at HH/FH interface in HH(1-x)/FH(x) composites that also clearly visualize from fig 5b. The energy barrier or offset, ΔE, between CBM of HH and FH acts as an energy filter for conduction electrons within the conduction band (CB) of HH. The height of this energy barrier, ΔE, depends on the CBM position of the FH phase. The CBM of FH inclusions usually depends on the size of the FH inclusions under quantum confinement regime. Therefore, the relative reductions in carrier density measured in HH(1-x)/FH(x) composites in $Zr_{0.7}Hf_{0.3}Ni_{1+x}Sn$ with x=0.03 and 0.05 around 300 K correspond to the fraction of low energy conduction electrons from the

CB of the HH matrix trapped by the energy barrier, ΔE, at the HH/FH interfaces. The fraction of low energy electrons trapped by the energy barrier increases with the increasing density of HH/FH interfaces within the composites, but at the same time decreases with the increasing size of FH inclusions (decreasing ΔE). In our synthesis conditions namely commercial arc melting technique, increasing the percentage of excess elemental Ni atoms in the starting compositions leads to the formation of various length scale size of FH inclusions varying from nano- to meso-scale length which form a mixture of small and large size FH inclusions in the bulk HH matrix and hence leads to an entirely complex transport behavior. In addition to band off-set minimization for the optimization of electronic transport, such kind of composites lead to the generation of all scale hierarchal architecturing features which covers a large range of wavelength scattering to reduce the thermal conductivity. A schematic showing with range of phonon scattering is presented in fig. 5c.

The temperature dependence of the power factor of HH (1-x)/FH(x) composites in $Zr_{0.7}Hf_{0.3}Ni_{1+x}Sn$ is presented in fig 4 (c). Interestingly, the composites with x=0.03 and x=0.05 exhibit large power factor compared to parent HH phase matrix. The highest power factor was optimized to be ~ 30.7 x 10^{-4} W m^{-1} K^{-2} at 773 K for HH (97%)/FH(3%) composite which is ~ 170 % larger value than parent HH matrix. This large enhancement in the power factor is ascribed to the observed unusual simultaneous increase in Seebeck coefficient and electrical conductivity of the composite.

3.4 Thermal transport properties

Another remarkable finding of this work is the fact that in addition to the increase in the power factor, the total thermal and lattice thermal conductivities of these HH(1- x)/FH(x) composites are also reduced when compared to bulk HH matrix (fig. 6a and 6d). The thermal conductivity is

calculated by taking the product of diffusivity and specific heat and density of the sample. These data for the samples are shown in the supplementary information as Fig. S2 and Fig. S3 respectively. Figure 6 (a) displays the temperature dependence of total thermal conductivity κ (T) all HH(1-x)/FH(x) composites in $Zr_{0.7}Hf_{0.3}Ni_{1+x}Sn$. Regardless to the temperature, the total thermal conductivity decreases with increasing concentration of FH inclusions in HH matrix. Interestingly, the total thermal conductivity, κ also decreases with rising temperature indicating that phonon conductivity dominates. The lowest thermal conductivity (~ 2.1 W m^{-1} K^{-1} at 773K) was observed for HH(90%)/FH(10%) in $Zr_{0.7}Hf_{0.3}Ni_{1.10}Sn$ sample. This corresponds to ~ 33 % reduction of the total thermal conductivity of the parent HH matrix. This drastic reduction in the thermal conductivity can be ascribed to an efficient phonon scattering at multiple length scale grains and phase boundaries.

The lattice thermal conductivity was obtained by subtracting the electronic thermal conductivity from the total measured thermal conductivity.[62] The Wiedemann-Franz law invoke to calculate the electronic thermal conductivity by a relation $\kappa_e = L\sigma T$, where L is Lorentz number, σ, the electrical conductivity and T, the temperature in K. The temperature dependent Lorenz number[63] and the bipolar contribution was taken into account by assuming $\kappa_{lattice} \sim 1/T$.[64] Figure 6 (c) represents the temperature dependent electronic thermal conductivity of the HH(1-x)/FH(x) composites. The κ_e is increasing with rising temperature for all the samples consistently with the increase in the electrical conductivity. The calculated lattice thermal conductivity of the HH(1-x)/FH(x) composites as a function of temperature is displayed in fig 6 (d). We observe that the lattice thermal conductivity decreases with increasing temperature, showing trend similar to the total thermal conductivity. Thus, reduction in total thermal conductivity is primarily due to drastic reduction in the lattice thermal conductivity. The observed reduction in the lattice thermal conductivities of HH(1-x)/FH(x) composites is attributed to the ability of multiple coherent nanometer scale HH/FH phase boundaries

within the composites to effectively scatter mid frequency phonons in addition to the typical scattering of mid-to-long wavelength phonons at grain boundaries.

3.4 Thermoelectric figure of merit:

The temperature dependence of ZT of all the HH(1-x)/FH(x) composites in $Zr_{0.7}Hf_{0.3}Ni_{1+x}Sn$ is presented in fig 7. Regardless of the temperature, the ZT of the HH(1-x)/FH(x) composites increases initially with increasing FH fractions upto x=0.05. Interestingly, the ZT increases with rising temperature for all the composites. However, highest ZT ≈ 0.96 at temperature of 773 K was realized for the HH (97%)/FH(3%) composite in $Zr_{0.7}Hf_{0.3}Ni_{1.03}Sn$ which is significantly enhanced than ZT ≈ 0.27 at 773 K for parent HH matrix phase. Thus combining a large value in the Seebeck coefficient (~ -158 μVK^{-1} at 773 K) and high electrical conductivity (~12.3 x 10^2 S m^{-1} at 773 K), together with low value of thermal conductivity (i.e.~ 2.4 W m^{-1} K^{-1} at 773 K), the ZT of the HH (97%)/FH(3%) composite in $Zr_{0.7}Hf_{0.3}Ni_{1.03}Sn$ was obtained to be about ~0.96 at 773 K which is ~ 250 % improvement than that of parent HH matrix phase. The HH (1-x)/FH(x) composite with x=0.1 which is metallic, although exhibit a reduced thermal conductivity, their high ZT could not be optimized because of their very low Seebeck coefficient and low power factor. Thus large level of FH inclusions in the matrix is not beneficial for optimizing high ZT.

3.5 Calculation of effective thermoelectric parameters via Bergman-Fel Effective Medium Model

Bergman-Fel effective medium model is used to calculate the effective value of thermoelectric parameters.[38,39] This model predicts the value of effective electrical conductivity $\sigma_{(E)}$, effective thermal conductivity $\kappa_{(E)}$ and effective Seebeck coefficient $\alpha_{(E)}$ for a binary composite containing a randomly dispersed inclusions of nearly spherical in shape within a matrix medium. If one assumes a

matrix medium HH as A and inclusion of FH as B in the present study and σ_A and σ_B the electrical conductivities, α_A and α_B the Seebeck coefficients, κ_A and κ_B as the thermal conductivities of the constituents A & B respectively, then the effective values of σ_E, κ_E and α_E for such composite can be describe as:

$$\sigma_E = \sigma_A + \frac{\phi}{D}\left(\frac{\delta_\sigma}{d_{BA}} + \frac{1-\phi}{3}\frac{\sigma_A}{d_A}\right) \quad \text{---------- (3)}$$

$$\kappa_E = \kappa_A + \left(\frac{\delta_\kappa}{d_{BA}} + \frac{1-\phi}{3}\frac{\kappa_A}{d_A}\right) \quad \text{---------- (4)}$$

$$\alpha_E = \left[\alpha_A\sigma_A + \frac{\phi}{D}\left(\frac{\delta_{\alpha\sigma}}{d_{BA}} + \frac{1-\phi}{3}\frac{\alpha_A\sigma_A}{d_A}\right)\right]\frac{1}{\sigma_E} \quad \text{---------- (5)}$$

Where φ is the volume fraction of Phase B and

$$\delta_\sigma \equiv \sigma_B - \sigma_{A,}\delta_\kappa \equiv \kappa_B - \kappa_{A,}$$

$$d_A \equiv \frac{\sigma_A\kappa_\partial}{T} - (\alpha_A\sigma_A)^2, d_{BA} \equiv \frac{\delta_\sigma\delta_\kappa}{T} - \delta_{\alpha\sigma}^2$$

and

$$D \equiv \left(\frac{\delta_\sigma}{d_{BA}} + \frac{1-\phi}{3}\frac{\sigma_A}{d_A}\right)\left(\frac{\delta_\kappa}{Td_{BA}} + \frac{1-\phi}{3}\frac{\kappa_A}{Td_A}\right) - \left(\frac{\delta_{\alpha\sigma}}{d_{BA}} + \frac{1-\phi}{3}\frac{\alpha_A\sigma_A}{d_A}\right)^2$$

For calculating the effective TE parameters for these composites, the volume fractions of 0, 3.2, 5.6 and 12.3% were taken for x=0, 0.03, 0.05 and 0.10 of FH inclusions in HH matrix respectively. The electrical conductivity, Seebeck coefficient and thermal conductivity of FH were measured from 323 to 773 K as shown inset of fig 4e, 4b and 6b respectively. By using Eq. (3), the σ_E for all of samples HH/FH composites were calculated and plotted in Fig. 4d. Similarly, κ_E and α_E were calculated by using eq. (4 & 5) as represented in fig.6 b and 4d respectively. The calculated effective thermoelectric parameters are compared with the experimentally obtain data for these composites and were found that a slightly deviated trends of α_E and σ_E upto 5.6% volume fraction of FH inclusions in composites were noticed. However, the magnitudes are entirely different which could be most

possibly due to varying size of FH inclusions ranging from submicron to nano sizes rather than being micron-sized inclusion phase as assumed in this model. For 10% FH inclusions, system becomes more like metallic in nature rather than semiconducting and hence loses its scope to be fitted in this model. The deviation in calculated effective thermoelectric parameters to present composite is attributed due to the filtering effect and interface boundary scattering. The filtering and interface boundary scattering were not assumed in this model and hence supports the violation of the model in the present study.

The transport properties of these submicron/nano–composites are affected by the size and distribution of FH inclusions. It is important to mention that these composites contains metallic FH inclusion exhibit a rather high α (fig. 4a) without changing the carrier concentration in comparison to the bulk HH matrix. The exact reason for this result is not yet clearly known. However, it could be an energy filtering mechanism, similar to that proposed by Faleev et al.[59] In the present work, low energy carriers might have filtered out by the scattering at potential barrier created at the interface between HH and metallic FH phases and thus enhancing α in these composites in comparison to bulk HH matrix. Thus, the all scale hierarchical architecturing for size and density of the FH inclusions could be a vital factor responsible for the enhancement of ZT.

3.7 Compatibility Factor :

Apart from the high thermoelectric figure of merit (ZT), another important parameter that play a vital role in the formation of thermoelectric devices is known as thermoelectric compatibility factor (s). In 2003, Snyder et al.[65] suggested this new physical parameter which describes the applicability of the materials to be used as a segmented couple for the thermoelectric device in power generation.

The thermoelectric compatibility factor (s) is the function of temperature and it depends upon the Seebeck coefficient (α), given as

$$s = \frac{\sqrt{1+ZT}-1}{\alpha T} \quad \text{----------} \quad (6)$$

where α is Seebeck coefficient in volts and T is temperature in Kelvin.

The evaluation of s in thermoelectric materials is needed to find out the possibility of the counterpart of the TE device and also required to achieve maximum TE efficiency. As, two different materials may be used in the segmented thermoelectric generator, if their thermoelectric compatibility factor are same or less than a factor of 2.[66-68]

The compatibility factor of $Zr_{0.7}Hf_{0.3}Ni_{1.03}Sn$ (-3.2 V^{-1} at 773K) is large as compare to the normal HH $Zr_{0.7}Hf_{0.3}NiSn$ (-1.5 V^{-1} at 773K). Also, the compatibility factor of $Zr_{0.7}Hf_{0.3}Ni_{1.03}Sn$ is high as compare to the other state-of-the art n-type TE materials. Hence, $Zr_{0.7}Hf_{0.3}Ni_{1.03}Sn$ is a suitable n-type material for segmentation with broad range of other state-of-the art TE materials to gain highest efficiency benefit for the thermoelectric devices used in power generation.[69] Thus, the dual advantages of reasonably high ZT and high value of compatibility factor made $Zr_{0.7}Hf_{0.3}Ni_{1.03}Sn$ materials to be the good material for segmentation with other n-type TE materials.

4. Concluding Remark and Future Prospects:

All scale hierarchical architecturing has been designed for the first time to enhance the thermoelectric performance of submicron/nano-composites of HH and FH based thermoelectric materials via compositional engineering approach. The HH (1-x)/FH(x) composites in compositions $Zr_{0.7}Hf_{0.3}Ni_{1+x}Sn$ ($0.0 \leq x \leq 0.10$) were sucessesfully synthesized employing arc melting followed by spark plasma sintering (SPS) deriving a wide size range of FH inclusions within the HH matrix. A

high ZT ~ 0.96 at 773K was optimized for the composition $Zr_{0.7}Hf_{0.3}Ni_{1.03}Sn$ which is ~250% higher in comparison to that observed for parent HH $Zr_{0.7}Hf_{0.3}NiSn$. This increase in ZT was observed due to the significant decrease in κ (~34% as compared to its bulk counterpart) and simultaneous improvement in power factor (~170% as compared to its bulk counterpart). Increasing FH fraction derives a wide range of variation in the sizes of FH phase which covers all length scales phonon scattering via hierarchical architecturing from atomic-scale, lattice disorder and nanoscale endotaxial FH precipitates to mesoscale grain boundaries and interfaces for significantly reducing the thermal conductivity. The enhancement of Seebeck coefficient is attributed to the combined effect of low energy electron filtering and electron injecting phenomenon. Further appropriate doping and nanostructuring in present optimized composition to increase ZT will be Future Avenue of this research. At the end of our concluding remarks, we strongly believe that the strategy of varying compositions of half-Heusler materials in a controlled way may derive several other off-stoichiometric compositions of half-Heusler with even higher ZT and such all scale hierarchical architecturing derived by compositional engineering approach may be extended to so many other explored state-of-the-art thermoelectric materials for enhancing their high thermoelectric performance.

Acknowledgement

This work was supported by CSIR-TAPSUN (NWP- 54) programme entitled "Novel approaches for solar energy conversion under technologies and products for solar energy utilization through networking." The authors are grateful to the Director, Prof. R. C. Budhani (Director, CSIR-NPL), for his constant mentoring and support for this project. The authors thank Dr. S.S. Rajput (CSIR-NPL) and Dr. Jiji Pullikotil (CSIR-NPL) for their continuous encouragement. We acknowledge Dr. Sunil Pandey (NIMS University, Jaipur) for providing the room temperature Hall

data. The authors AB and NSC acknowledge the financial support from UGC-CSIR and CSIR respectively. The technical support rendered by Mr. Bathula Sivaiah, Mr. Radhey Shyam, and Mr. Naval Kishor Upadhyay is gratefully acknowledged.

References:

1. C. J. Vineis, A. Shakouri, A. Majumdar, M. G. Kanatzidis, *Adv. Mater*, 2010, **22**, 3970.
2. G. J. Snyder, E. S. Toberer, *Nat. Mater.,*2008, **7**, 105.
3. K. F. Hsu, S. Loo, F. Guo, W. Chen, J. S. Dyck, C. Uher, T. Hogan, E. K. Polychroniadis and M. G. Kanatzidis, *Science*, 2004, **303**, 818.
4. J. P. Heremans, V. Jovovic, E. S. Toberer, A.Saramat, K. Kurosaki, A.Charoenphakdee, S. Yamanaka, G. J. Snyder, *Science*, 2008, **321**, 554.
5. T. C. Harman, P. J. Taylor, M. P. Walsh, B. E.LaForge, *Science*, 2002, **297**, 2229.
6. A. I. Hochbaum, R. K. Chen, R. D. Delgado, W. J. Liang, E. C. Garnett, M.Najarian, A. Majumdar, P. D. Yang, *Nature,* 2008, **451**, 163.
7. B. Poudel, Q. Hao, Y. Ma, Y. C.Lan, A.Minnich, B. Yu, X. Yan, D. Z. Wang, A. Muto, D. Vashaee, X. Y. Chen, J. M. Liu, M. S.Dresselhaus, G. Chen, Z. F. Ren, *Science*, 2008, **320**, 634.
8. R. Venkatasubramanian, E. Siivola, T. Colpitts and B. O'Quinn, *Nature*, 2001, **413**, 597–602.
9. A. Banik, U. S. Shenoy, S. Anand, U. V. Waghmare, K. Biswas, *Chemistry of Materials*, 2015, **27**, 581-587.
10. S. N. Guin, A. Chatterjee, D. S. Negi, R. Datta, K. Biswas, *Energy & Environmental Science*, 2013, **6**, 2603-2608
11. S. N. Guin, V. Srihari, K. Biswas, *Journal of Materials Chemistry A*, 2015, **3**, 648-655.

12. A. Bhardwaj, D. K. Misra, J. J. Pulikkotil, S. Auluck, A. Dhar and R. C. Budhani,*Appl. Phys. Lett.*, 2012, **101**, 133103.
13. A. Bhardwaj, A. K. Shukla, S. R.Dhakate, D. K.Misra, *RSC Advances*, 2014, **5**, 11058-11070.
14. D. K. Misra, A. Bhardwaj and S. Singh, *J. Mater. Chem. A*, 2014, **2**, 11921-11931.
15. A. Bhardwaj, D. K. Misra, *J. Mater. Chem. A*, 2014, **2**, 20980-20989.
16. A. Bhardwaj, N. S. Chauhan, D. K. Misra, *J. Mater. Chem. A,* 2015, **3**, 10777-10786.
17. D. K. Misra, A. Rajput, A. Bhardwaj, N. S. Chauhan, S. Singh, *App. Phys. Lett.,* 2015, **106**, 103901.
18. Y. Pei, H. Wang and G. J. Snyder, *Adv. Mater.*, 2012, **24**, 6124.
19. J. Androulakis, K. F. Hsu, R. Pcionek, H. Kong, C. Uher, J. J. D'Angelo, A. Downey, T. Hogan and M. G. Kanatzidis,*Adv. Mater.*, 2006, **18**, 1170.
20. K. Ahn, K. Biswas, J. He, I. Chung, V. Dravid and M. G. Kanatzidis, *Energy Environ. Sci.*, 2013, **6**, 1529.
21. Y. Pei, J. L. Falk, E. S. Toberer, D. L. Medlin and G. J. Snyder, *Adv. Funct. Mater.*, 2011, **21**, 241–249.
22. A. Bhardwaj, A. Rajput, A. K.Shukla, J. J.Pulikkotil, A. K. Srivastava, A. Dhar, G.Gupta, S.Auluck, D. K. Misra and R. C. Budhani, *RSC Adv.*, 2013, **3**, 8504.
23. A. Bhardwaj and D. K. Misra, *RSC Adv.*, 2014, **4**, 34552.
24. Y. Pei, A. D. LaLonde, S. Iwanaga and G. J. Snyder, *Energy Environ. Sci.*, 2011, **4**, 2085-2089.
25. A. J. Minnich, M. S. Dresselhaus,Z. F. Ren and G. Chen, *Energy Environ. Sci.*, 2009, **2**, 466.
26. J. He, M. G. Kanatzidis and V. P. Dravid, *Materials Today,* 2013, **16**, 5.
27. L. -D. Zhao, V. P. Dravid and M. G. Kanatzidis, *Energy Environ. Sci.*, 2014, **7**, 251–268.
28. K. Biswas, J. Q. He, Q. C. Zhang, G. Y. Wang, C. Uher, V. P. Dravid and M. G. Kanatzidis, *Nat. Chem.*, 2011, **3**, 160–166.

29. K. Biswas, J. Q. He, G. Y. Wang, S. H. Lo, C. Uher, V. P. Dravid and M. G. Kanatzidis, *Energy Environ. Sci.*, 2011, **4**, 4675–4684.

30. K. Biswas, J. Q. He, I. D. Blum, C. I. Wu, T. P. Hogan, D. N. Seidman, V. P. Dravid and M. G. Kanatzidis, *Nature*, 2012, **489**, 414–418.

31. L. D. Zhao, S. Hao, S. H. Lo, C. I. Wu, X. Zhou, Y. Lee, H. Li, K. Biswas, T. P. Hogan, C. Uher, C. Wolverton, V. P. Dravid and M. G. Kanatzidis, *J. Am. Chem. Soc.*, 2013, **135**, 7364.

32. Y. Lee, S. H. Lo, J. Androulakis, C. I. Wu, L. D. Zhao, D. Y. Chung, T. P. Hogan, V. P. Dravid and M. G. Kanatzidis, *J. Am. Chem. Soc.*, 2013, **135**, 5152– 5160.

33. P. F. P. Poudeu, J. D'Angelo, A. D. Downey, J. L. Short, T. P. Hogan and M. G. Kanatzidis, *Angew. Chem., Int. Ed.*, 2006, **45**, 3835–3839.

34. J. Q. He, J. Androulakis, M. G. Kanatzidis and V. P. Dravid, *Nano Lett.*, 2012, **12**, 343–347.

35. Y. Lan, A. J. Minnich, G. Chen and Z. Ren, *Adv. Funct. Mater.*, 2010, **20**, 357–376

36. B. Yu, M. Zebarjadi, H. Wang, K. Lukas, H. Z. Wang, D. Z. Wang, C. Opeil, M. Dresselhaus, G. Chen and Z. F. Ren, *Nano Lett.*, 2012, **12**, 2077–2082.

37. Y. Z. Pei, H. Wang, Z. M. Gibbs, A. D. LaLonde and G. J. Snyder, *NPG Asia Mater.*, 2012, **4**, 28.

38. D. J. Bergman and O. J. Levy, *J. Appl. Phys.*, 1991, **70**, 6821.

39. D. J. Bergman and L. G. Fel, *J. Appl. Phys.*, 1999, **85**, 8205.

40. J. P. Heremans and C. M. Jaworski, *Appl. Phys. Lett.*, 2008, **93**,122107.

41. F. Brochin, B. Lenoir, X. Devaux, R. M. -Lonze, H. Scherrer, *J. App Phys.*, 2000, **88**, 3269.

42. (a) J. R. Sootsman, H. Kong, C. Uher, J. J. D'Angelo, C. I. Wu, T. P. Hogan, T. Caillat and M. G. Kanatzidis, *Angew. Chem., Int. Ed.*, 2008, **47**, 8618. (b) K. Ahn, M. K. Han, J. Q. He, J. Androulakis, S. Ballikaya, C. Uher, V. P. Dravid and M. G. Kanatzidis, *J. Am. Chem. Soc.*, 2010, **132**, 5227–5235.

43. (a) G. Rogl,A. Grytsiv,P. Rogl,E. Bauer,M. Hochenhofer,E. Schafler, *Acta Materialia,* 2014, **76**, 434–448. (b) B. C. Sales, D. Mandrus, R. K. Williams, *Science,*1996, **272**, 1325. (c) R. C. Mallik, R.Anbalagan, G. Rogl, E. Royanian, P. Heinrich, E. Bauer, P. Rogl and S. Suwas, *Acta Materialia*, 2013, **61**, 6698–6711. (d) R. C. Mallik, R. Anbalagan, K. K. Raut, A. Bali, E. Royanian, E. Bauer, G. Rogl, P. Rogl, *Journal of Physics: Condensed Matter*, 2013, **25**, 105701. (e) G. Rogl, A. Grytsiv, P. Rogl, N. Peranio, E. Bauer, M. Zehetbauer, O. Eibl, *Acta Materialia*, 2014, **63**, 30–43.

44. (a) B. Poudel, Q. Hao, Y. Ma, Y. Lan, A. Minnich, B. Yu, X. Yan, D. Wang, A. Muto, D. Vashaee, X. Chen, J. Liu, M. S. Dresselhaus, G. Chen and Z. Ren, *Science*, 2008, **320**, 634. (b) S. Yu, J. Yang, Y. Wu, Z. Han, J. Lu, Y. Xie and Y. Qian, *J. Mater. Chem.*, 1998, **8**,1949. (c) J. Shen, T. Zhu, X. Zhao, S. Zhang, S. Yanga and Z. Yina, *Energy Environ. Sci.*, 2010, **3**, 1519. (d) M. E. Anderson, S. S. N. Bharadwaya and R. E. Schaak, *J. Mater. Chem.*, 2010, **20**, 8362. (e) S. Sumithra, N. J. Takas, D. K. Misra, W. M. Nolting, P. F. P. Poudeu and K. L. Stokes, *Adv. Energy Mater.*, 2011, **1**, 1141.

45. (a) M. Bashir, A. Bashir, S. M. Said , M.Faizul, M.Sabri, D. A.Shnawah,M. Hamid, *Renewable and Sustainable Energy,* 2014, **37**, 569–584. (b) S. N. Girard, X. Chen, F. Meng, A. Pokhrel, J. Zhou, L. Shi and S. Jin, *Chem. Mater.*, 2014, **26**, 5097–5104. (c) W. Liu, X. F. Tang, H. Li, J. Sharp, X. Zhou, and C.Uher,*Chem. Mater.*, 2011, **23**, 5256–5263. (d) Q. Zhang, J. He, X. B. Zhao, S. N. Zhang, T. J. Zhu, H. Yin and T. M.Tritt,*J. Phys. D: Appl. Phys.*, 2008, **41**, 185103.

46. (a) P. Sahoo, Y. Liu, P. F. P. Poudeu, *J. Mater. Chem. A*, 2014, **2**, 9298-9305. (b) Y. Liu, A. Page, P. Sahoo, H. Chi, C. Uher, P. F. P. Poudeu, *Dalton Trans*, 2014, **43**, 8094-8101. (c) J. Makongo, X. Zhou, D. K. Misra, C. Uher, P. F. P. Poudeu, *J. Sol. Stat. Chem.*, 2013, **201**, 280-287. (d) Y. Liu, P.Sahoo, J. P. A.Makongo, X. Zhou, S. -J. Kim, H. Chi, C. Uher, X. Pan, P. F. P. Poudeu, *J. Am. Chem. Soc.*, 2014, **135**, 7486-7495. (e) P. Sahoo, Y. Liu, J. P. A. Makongo, X.-Li Su, S. J. Kim, N.

Takas, H. Chi, C. Uher, X. Pan, P. F. P. Poudeu, *Nanoscale*, 2014, **5**, 9419-9427. (f) J. P. A. Makongo, D. K. Misra, X. Zhou, A. Pant, M. R. Shabetai, X. Su, C. Uher, K. L. Stokes, P. F. P. Poudeu, *J. Am. Chem. Soc.*, 2011, **133**, 18843-18852. (g) R. A. Downie, R. I. Smith, D. A. MacLaren, and J.-W. G. Bos, *Chem. Mater.* 2015, **27**, 2449−2459. (h) R. A. Downie, D. A. MacLaren and J.-W. G. Bos, *J. Mater. Chem. A*, 2014, **2**, 6107. (i) C. S. Birkel, W. G. Zeier, J. E. Douglas, B. R. Lettiere, C. E. Mills, G. Seward, A. Birkel, M. L. Snedaker, Y. Zhang, G. J. Snyder, T. M. Pollock, R. Seshadri and G. D. Stucky, *Chem. Mater.,* 2012, **24**, 2558–2565. (j) C. S. Birkel, J. E. Douglas, B. R. Lettiere, G. Seward, N. Verma, Y. Zhang, T. M. Pollock, R. Seshadri and G. D. Stucky, *Phys. Chem. Chem. Phys.*, 2013, **15**, 6990. (k) J. E. Douglas, C. S. Birkel, M. -S. Miao, C. J. Torbet, G. D. Stucky, T. M. Pollock and R.Seshadri, *Appl. Phys. Lett.*, 2012, **101**, 183902. (l) V.V. Romaka, P. Rogl, L. Romaka, Y. Stadnyk, A. Grytsiv, O. Lakh, V. Krayovskii, *Intermetallics*, 2013, **35**, 45–52. (m) J. E. Douglas, C. S. Birkel, N. Verma, V. M. Miller, M. -S. Miao, G. D. Stucky, T. M. Pollock and R. Seshadri, *J. Appl. Phys.,* 2014, **115**, 043720. (n) J. E. Douglas, P. A. Chater, C. M. Brown, T. M. Pollock and R. Seshadri, *J. Appl. Phys.,* 2014, **116**, 163514

47. S. Sakurada and N. Shutoh, *Appl. Phys. Lett.*, 2005, **86**, 082105.
48. (a) S. R. Culp, S. J. Poon, N. Hickman, T. M. Tritt and J. Blumm, *Appl. Phys. Lett*., 2006, **88**, 042106. (b) S. W. Kim, Y. Kimura and Y. Mishima, *Intermetallics*, 2007, **15**, 349–356. (c) H. Muta, T. Kanemitsu, K. Kurosaki and S. Yamanaka, *J. Alloys Compd*., 2009, **469**, 50–55.
49. D. Rowe, CRC Handbook of Thermoelectrics, Boca Raton, **1995**.
50. X. Yan, W. Liu, H. Wang, S. Chen, J. Shiomi, K. Esfarjani, H. Wang, D. Wang, G. Chen and Z. Ren, *Energy Environ. Sci*., 2012, **5**, 7543–7548.

51. (a) H.-H. Xie, C. Yu, T.-J. Zhu, C.-G. Fu, G. J. Snyder and X.-B. Zhao, *Appl. Phys. Lett.*, 2012, **100**, 254104. (b) Y. W. Chai and Y. Kimura, *Appl. Phys. Lett*., 2012, **100**, 033114. (c) J. P. A. Makongo, D. K. Misra, J. R. Salvador, N. J. Takas, G. Wang, M. R. Shabetai, A. Pant, P. Paudel, C. Uher, K. L. Stokes and P. F. P. Poudeu, *J. Solid State Chem*., 2011, **184**, 2948–2960.
52. X. Yan, W. Liu, H. Wang, S. Chen, J. Shiomi, K. Esfarjani, H. Wang, D. Wang, G. Chen and Z. Ren, *Energy Environ. Sci.*, 2012, **5**, 7543–7548.
53. K. Biswas, J. He, I. D. Blum, C.-I. Wu, T. P. Hogan, D. N. Seidman, V. P. Dravid and M. G. Kanatzidis, *Nature*, 2012, **489**, 414–418.
54. Y. W. Chai, T. Oniki and Y. Kimura, *Acta Materialia*, 2015, **85**, 290–300
55. D. Keazler, D. Cahen and J. Lbers, POLSQ FORTRAN program, Northwestern University, Evanston, IL, **1984**.
56. (a) W. Jeitschko, *Metall. Trans*., 1970, **1**, 3159–3162. (b) C. B. H. Evers, C. G. Richter, K. Hartjes and W. Jeitschko, *J. Alloys Compd*., 1997, **252**, 93–97.
57. J. Pierre, R. V. Skolozdra, Y. K. Gorelenko and M. Kouacou, *J. Magn. Magn. Mater*., 1994, **134**, 95–105.
58. (a) V. V. Romaka, P. Rogl, L. Romaka, Y. Stadnyk, N. Melnychenko, A. Grytsiv, M. Falmbigl and N. Skryabina, *J. Solid State Chemistry*, 2013, **197**, 103–112. (b) K. Kirievsky, Y. Gelbstein, D. Fuks, *J. Solid State Chemistry*, 2013, **203**, 247–254. (c) Y. W. Chai, Y. Kimura, *Appl. Phys. Lett*., 2012, **100**, 033114.
59. S. V. Faleev and F. Leonard, *Phys. Rev. B*., 2008, **77**, 214304.
60. G. S. Nolas, J. Sharp and H. J. Goldsmid, Thermoelectrics: Basic Principles and New Materials Developments, *Springer*, Berlin **2001**.

61. L. I. Bytenskii, T. S. Gudkin , E. K. Iordanishvili, S. A. Kazmin, V. I. Kaidanov and S. A. Nemov, *Sov. Phys. Semicond.*, **1977**, 11, 894.

62. H. Kitagawa, M. Wakatsuki, H. Nagaoka, H. Noguchi, Y. Isoda, K. Hasezaki and Y. J. Noda, *Phys. Chem. Solids*, 2005, **66**, 1635.

63. W. S. Liu, B. P. Zhang, J. F. Li, H. L. Zhang and L. D. Zhao, *J. Appl. Phys.*, 2007, **102**, 103717.

64. L. D. Chen, X. Y. Huang, M. Zhou, X. Shi and W. B. Zhang, *J. Appl Phys.*, 2006, **99**, 064305.

65. G. J. Snyder and T. S. Ursell, *Phys. Rev. Lett.,* 2003, **91**, 148301.

66. G. J. Snyder, *Appl. Phys. Lett*., 2004, **84**, 2436.

67. E. Macia, *Phys. Rev. B*, 2004, **70**, 100201.

68. S. R. Brown, S. M. Kauzlarich, F.Gascoin, and G. Jeffrey Snyder, *Chem. Mater.*, 2006, **18**, 1873-1877

69. P. H. Ngan, D. V. Christensen, G. J. Snyder, Le. T. Hung, S. Linderoth, N. Van Nong, and N. Pryds, *Phys. Status Solidi A*, 2014, **211**, 9.

Figure Caption:

Figure 1. (a) X-ray diffraction (XRD) pattern of HH(1-x) / FH(x) composites in composition $Zr_{0.7}Hf_{0.3}Ni_{1+x}Sn$ (with x= 0, 0.03, 0.05 and 0.1) (b & c) the unit cell parameters of the HH phase and FH phase with increasing FH fraction (x) in HH(1-x) / FH(x) composites.

Figure 2(a-b). Ball and stick arrangement of half-Heusler (HH) and full-Heusler (FH) structure, respectively, illustrating the atomic arrangement (c) Schematic illustrating the formation of a Ni rich cluster through diffusion of Ni atoms into vacant sites. The thick solid line at the bottom indicates a unit cell of HH and light blue colored rectangle on the top shows full-Heusler. This diagram is viewed along $[1\ 0\ -1]_{HH}$ phase.

Figure 3: (a) Low- magnification TEM micrograph of $Zr_{0.7}Hf_{0.3}Ni_{1.03}Sn$ composite displaying two phase contrasts of HH and FH and inset shows the high resolution image of the marked rectangle which shows the nanoscale precipitates of FH. (b) Shows more clear view of $Zr_{0.7}Hf_{0.3}Ni_{1.03}Sn$ composite showing the various length of the FH inclusion with their lattice resolution (c) HRTEM image showing a coherent interface between the HH matrix and FH inclusion interface.

Figure 4: Temperature dependence of electronic transport properties of HH (1-x)/FH(x) composites in $Zr_{0.7}Hf_{0.3}Ni_{1+x}Sn$ (with x= 0, 0.03, 0.05, 0.1) including of FH phase along with their calculated effective electronic transport properties using Bergemen and Fel model (a & d) electrical conductivity (b & e) Seebeck coefficient (c & f) power factor.

Figure 5: The band structure alignment of HH and FH at the HH/FH interfaces. (a) displays the MOT diagram of formation of FH (MNiSn) due to the insertion of Ni into vacant tetrahedral site of HH phase (MNiSn). (b) relative energy band diagram for the H (1-x)/FH(x) composites in $Zr_{0.7}Hf_{0.3}Ni_{1+x}Sn$ showing the mechanism of the filtering of low energy electrons (from CB of HH) at the potential barrier, ΔE, (reducing elective carrier density) and spatial separation of high energy electrons (within CB of FH) at nanometer scale HH/FH heterojunctions. (c) all-scale hierarchical architectures covering wide range of phonon scattering resulting from varying grain sizes.

Figure 6: Temperature dependence of thermal transport properties of HH (1-x)/FH(x) composites in $Zr_{0.7}Hf_{0.3}Ni_{1+x}Sn$ (with x= 0, 0.03, 0.05, 0.1) and calculated effective total thermal conductivity using Bergemen and Fel model (a & b) total thermal conductivity and effective total thermal conductivity respectively and inset of b) show the total thermal conductivity of FH (c & d) the electronic and lattice thermal conductivity of all HH(1-x)/FH(x) composites.

Figure 7: Temperature dependence of thermoelectric figure of merit of of HH (1-x)/FH(x) composites in $Zr_{0.7}Hf_{0.3}Ni_{1+x}Sn$ (with x= 0, 0.03, 0.05, 0.1).

Figure 8: display the temperature dependent TE compatibility factor for n-type $Zr_{0.7}Hf_{0.3}Ni_{1+x}Sn$ ($0 \leq x \leq 0.10$) bulk submicron/nano-composites.

Table 1: Hall measurement data of HH (1-x)/FH(x) composites derived from the compositions $Zr_{0.7}Hf_{0.3}Ni_{1+x}Sn$ ($0.0 \leq x \leq 0.10$) at room temperature.

Nominal Composition	**Hall Coefficient (R_H) $\times 10^{-1}$ cm^3C^{-1}**	**Carrier conc. n (10^{19} cm^{-3})**	**Mobility μ ($cm^2V^{-1}s^{-1}$)**
$Zr_{0.7}Hf_{0.3}NiSn$	1.22	4.9	82.2
$Zr_{0.7}Hf_{0.3}Ni_{1.03}Sn$	3.54	1.7	215.1
$Zr_{0.7}Hf_{0.3}Ni_{1.05}Sn$	1.87	3.2	126.7
$Zr_{0.7}Hf_{0.3}Ni_{1.10}Sn$	0.58	10.3	108.1

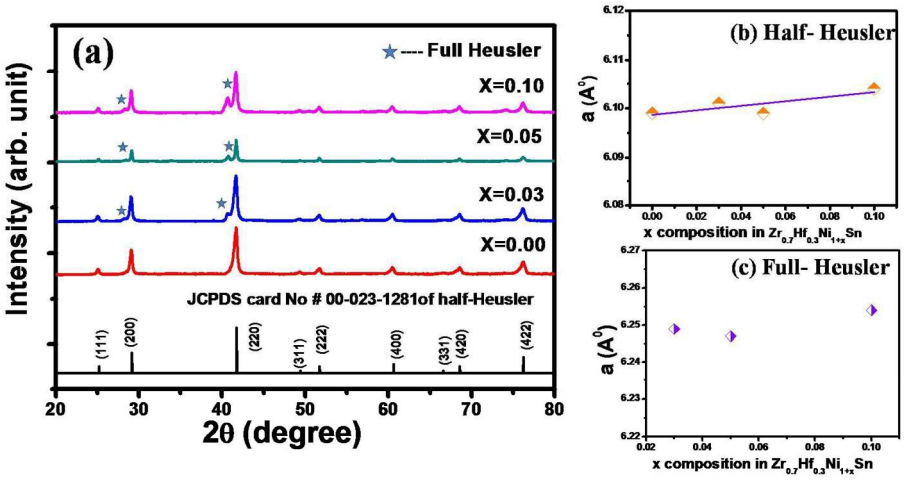

310x158mm (150 x 150 DPI)

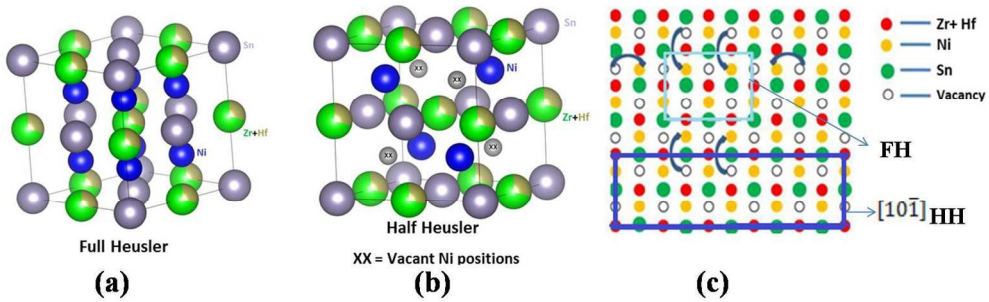

283x87mm (150 x 150 DPI)

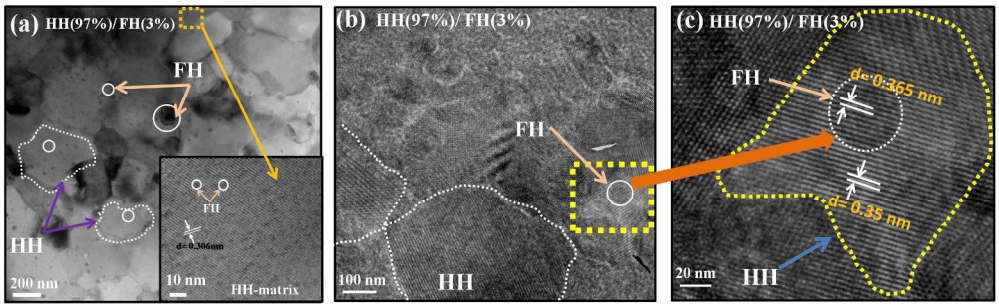

451x139mm (150 x 150 DPI)

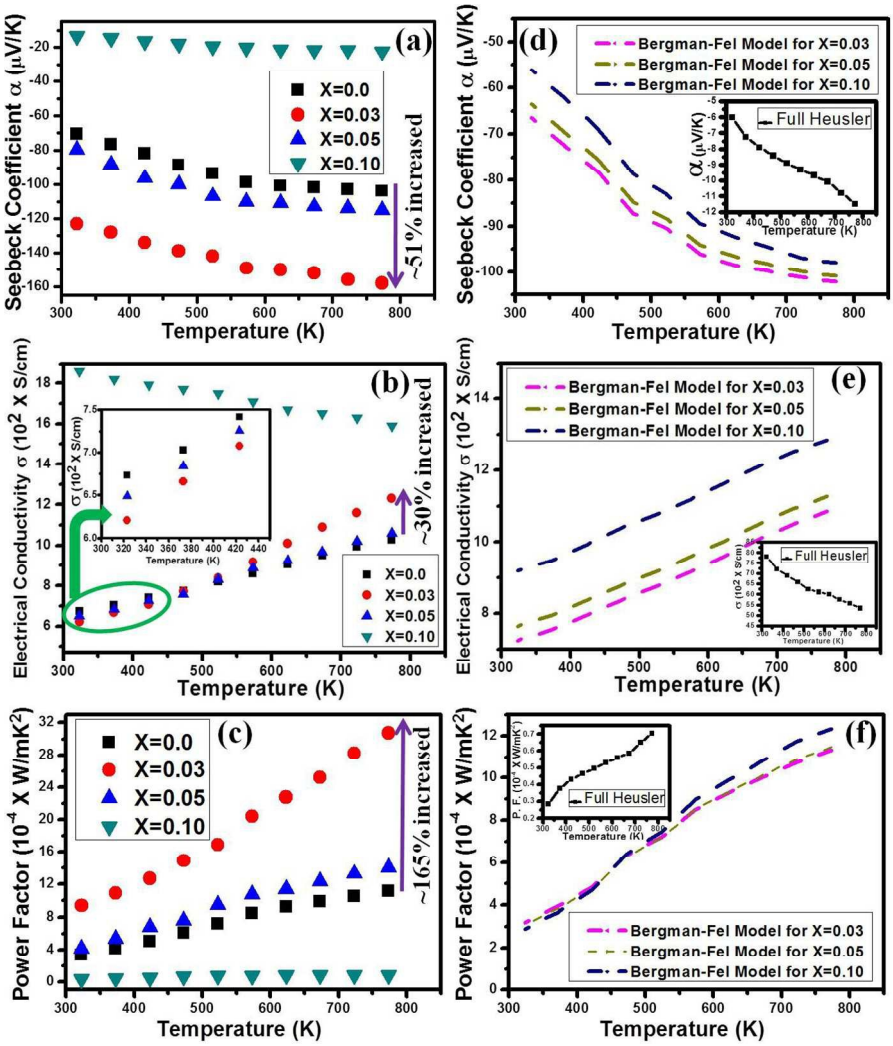

262x283mm (150 x 150 DPI)

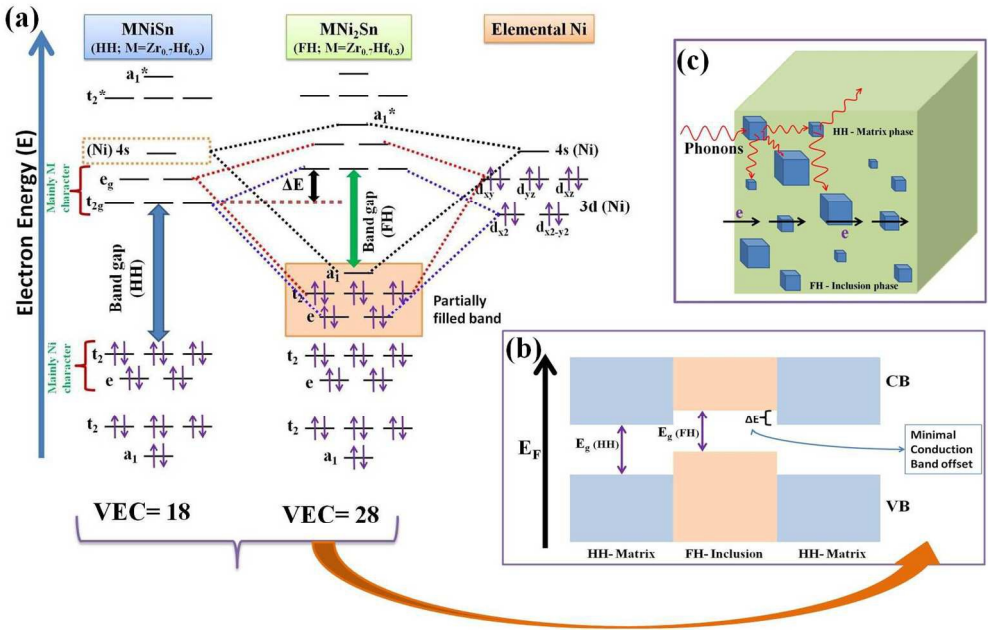

283x182mm (150 x 150 DPI)

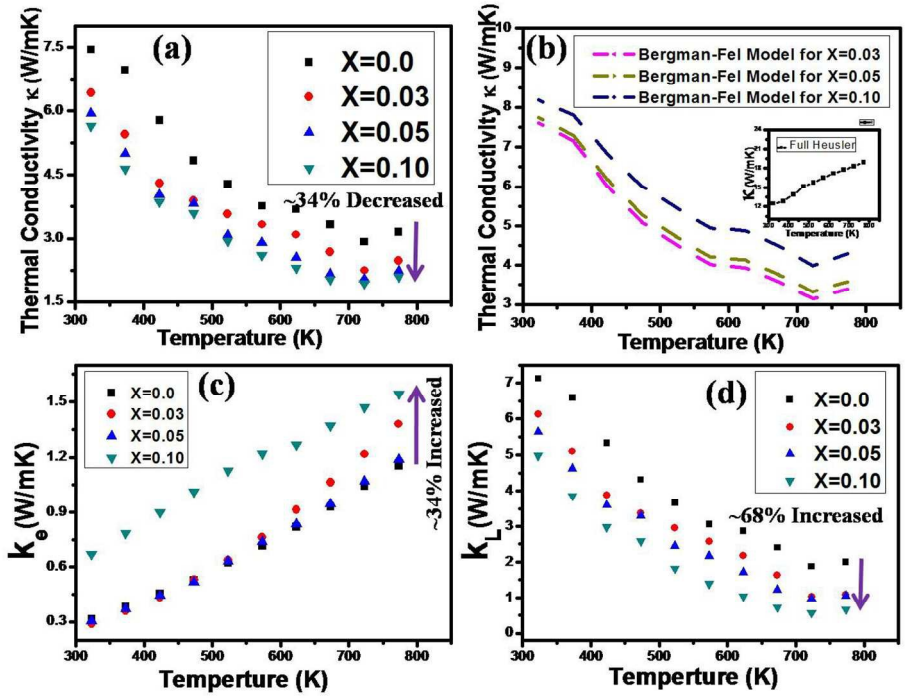

249x181mm (150 x 150 DPI)

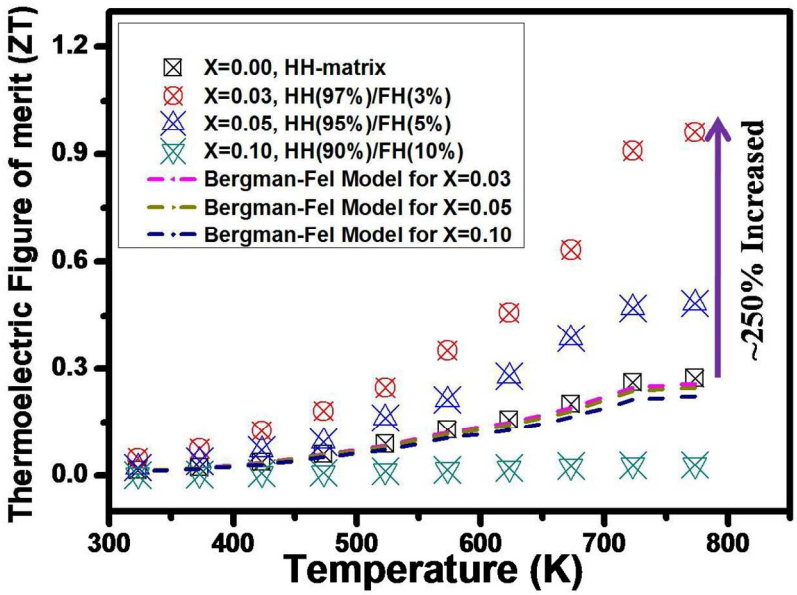

257x179mm (150 x 150 DPI)

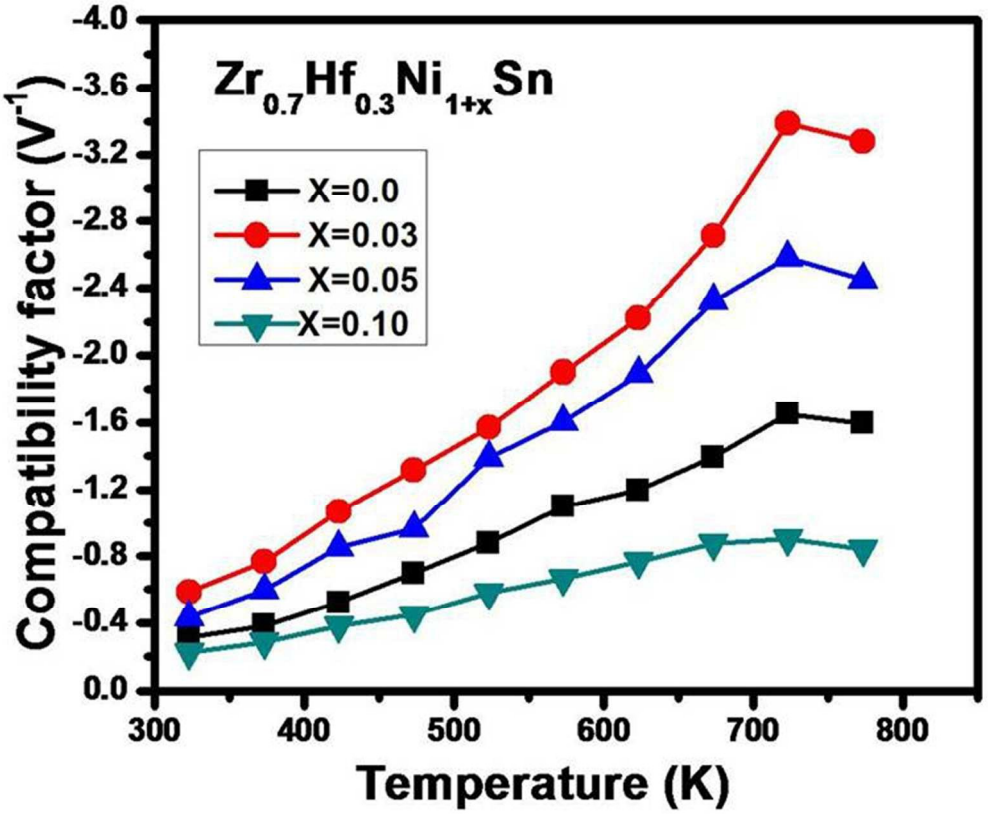

128x106mm (150 x 150 DPI)